supporting information to

Wind-driven evolution of the North Pacific subpolar gyre over the last deglaciation

William R Gray[1,2]*, Robert CJ Wills[3], James WB Rae[2], Andrea Burke[2], Ruza F Ivanovic[4], William HG Roberts[5], David Ferreira[6], Paul J Valdes[7]

[1]Laboratoire des Sciences du Climat et de l'Environnement (LSCE/IPSL), Gif-sur-Yvette, France
[2]School of Earth and Environmental Science, University of St Andrews, UK
[3]Department of Atmospheric Sciences, University of Washington, USA
[4]School of Earth & Environment, University of Leeds, UK
[5]Geography and Environmental Sciences, Northumbria University, UK
[6]Department of Meteorology, University of Reading, UK
[7]School of Geographical Sciences, University of Bristol, UK

*corresponding author: william.gray@lsce.ipsl.fr

Table of contents

Other supporting information not included in this file *- Dataset S1, Table S2*

Using planktic foraminiferal $\delta^{18}O$ to trace the gyre boundary

The $\delta^{18}O$ of the planktic foraminiferal calcite ($\delta^{18}O_{calcite}$) is a function of the $\delta^{18}O$ of seawater ($\delta^{18}O_{water}$, which is closely related to salinity), and the temperature dependant fractionation between calcite and water ($\delta^{18}O_{calcite-water}$); specifically, the fractionation between calcite and water is described by a fractionation factor ($\alpha_{calcite-}$

$_{water}$ = $[^{18}O/^{16}O]_{calcite}$ / $[^{18}O/^{16}O]_{water}$) which is related to temperature via,

$$1000 \ln \alpha_{calcite\text{-}water} = 18.03(10^3 T^{-1}) - 32.42$$

where T is temperature in Kelvin (Kim and O'Neil, 1997).

Our ability to use the planktic foraminiferal $\delta^{18}O_{calcite}$ to trace the gyre boundary comes from the dominance of the temperature signal over that of $\delta^{18}O_{water}$ in driving the meridional pattern of $\delta^{18}O_{calcite}$ across the basin; the temperature signal is 4-5 times greater than the $\delta^{18}O_{water}$ signal (Figure 1). As the spatial temperature pattern across the basin is primarily governed by the gyre circulation, with the steepest meridional temperature gradient (and thus meridional $\delta^{18}O_{calcite}$ gradient) at the gyre boundary, we can use the meridional profiles of temperature (and thus $\delta^{18}O_{calcite}$) to track the movement of the gyre boundary. Coupled climate models demonstrate a very tight coupling between the LGM-PI change in latitude of gyre boundary (defined where barotropic stream function = 0) and LGM-PI change in the latitude of maximum latitudinal gradient in sea surface temperature (SST) (Figure S1). As no mechanism exists to drive changes in $\delta^{18}O_{water}$ of the same magnitude as the changes in $\delta^{18}O_{calcite\text{-}water}$ fractionation from the large temperature difference between the gyres (Figure 1d), the temperature signal will always dominate over the $\delta^{18}O_{water}$ signal in determining the spatial pattern of $\delta^{18}O_{calcite}$ (Figure 1e) across the basin and the maximum meridional $\delta^{18}O_{calcite}$ gradient (Figure 1f); thus, while there are likely to be local changes in $\delta^{18}O_{water}$ across the basin, the steepest part of the meridional $\delta^{18}O_{calcite}$ gradient will always be determined by temperature, allowing us to use meridional profiles of $\delta^{18}O_{calcite}$ to track the position of the gyre boundary through time.

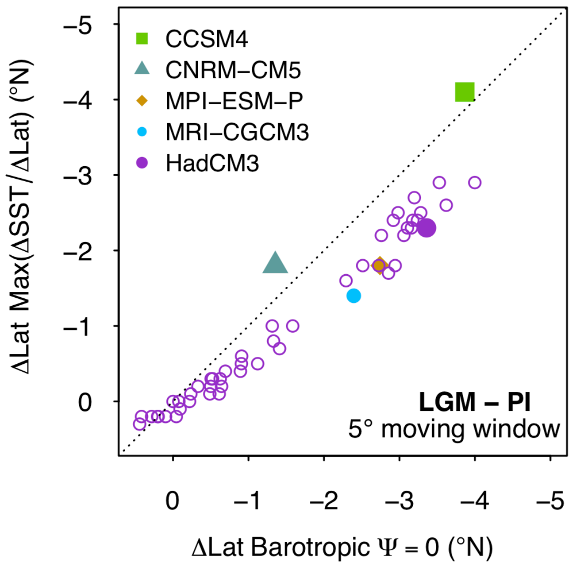

Figure S1 Modelled zonal mean LGM-pre-industrial (PI) change in latitude of gyre boundary (defined where barotropic stream function = 0) versus LGM-PI change in latitude of maximum meridional gradient in sea surface temperature (SST) within a 5° moving window; the close relationship demonstrates past changes in the position of the maximum gradient in SST/Lat (and thus ~$\delta^{18}O_{calcite}$/Lat) can be used to trace changes in the position of the gyre boundary.

We model the compiled $\delta^{18}O_{calcite}$ data (see below) as a function of latitude, using a Gaussian generalized additive model (GAM) (Wood, 2011; Wood *et al*., 2016) in the *mgcv* package in R (R core Team) at 100 yr timesteps from 18.5 to 10.5 ka (the time interval/resolution for which we have sufficient spatial and temporal coverage in our dataset; Figure 1),

$$\delta^{18}O_{calcite} = \beta_0 + f(\mathrm{Lat}) + \varepsilon$$

where β_0 is the intercept term, ε is random error, and f(Lat) is a smooth function, which can be represented as the sum of the underlying basis functions,

$$f(Lat) = \sum_{j=1}^{k} b_j(Lat)\beta_j$$

where b_j is the evaluation of the j^{th} basis function at the value of Lat, and β_j is the estimated coefficient or weight of that basis function. We sum over the weighted values of k basis functions (j = 1, 2, …, k), which comprise of reduced rank thin plate regression splines (Wood, 2011; Wood et al., 2016; Simpson, 2018). Here, k was set to 8, although the value of k has little effect on the smooth function. The smooth function is estimated by minimising the penalised sum of squares; the penalty term imposes smoothness by calculating the integrated square of the second derivative of the spline (Wood, 2011; Wood et al., 2016; Simpson, 2018),

$$penalty = \lambda \int f^{''}(Lat)^2 dLat$$

with the smoothness parameter (λ) controlling the extent to which the penalty term contributes to the likelihood of the model, with larger λ giving a smoother function (Wood, 2011; Wood et al., 2016; Simpson, 2018). The smoothness parameter was determined using Restricted Maximum Likelihood (REML, Reis and Ogden, 2009; Wood *et al*., 2016). Uncertainty envelopes on the fitted models (Figure 2) represent the 68% and 95% Bayesian credible intervals. The reader is directed to Simpson (2018) for a detailed overview of GAM methodology.

Figure S2 (below) GAM fits to $\delta^{18}O_{calcite}$ data as a function of latitude at 500 year timesteps from 18.5 to 10.5 ka (colours indicate age); the GAM fit to Holocene $\delta^{18}O_{calcite}$ data (10.5 ka) is shown in dark grey. The portion of the curve within the latitudinal band used to calculate the shift in gyre position (see Fig. S5) is shown by the solid line; at each timestep we calculate the latitudinal shift that minimises the Euclidean distance (along the y-axis) between the solid part of the coloured curve and the solid part of the grey curve. Data are the combined east-west dataset (marked ALL on Figure 4). Note, the reconstruction in Figure 5 uses time-steps of 100 years; here we show the meridional profiles at time-steps of 500 years for illustrative purposes.

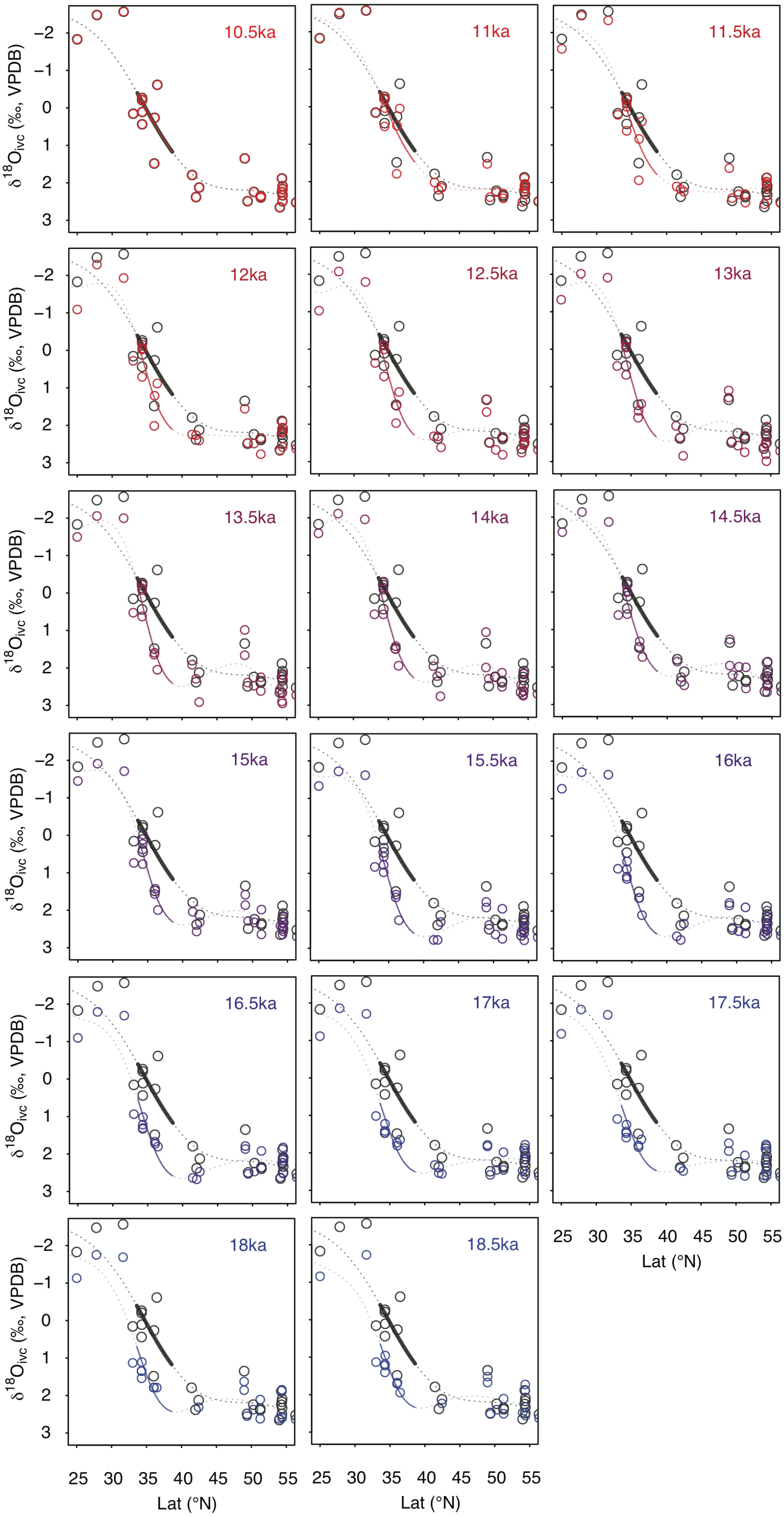

10.5ka
11ka
11.5ka
12ka
12.5ka
13ka
13.5ka
14ka
14.5ka
15ka
15.5ka
16ka
16.5ka
17ka
17.5ka
18ka
18.5ka
δ18Oivc (‰, VPDB)
Lat (°N)

89

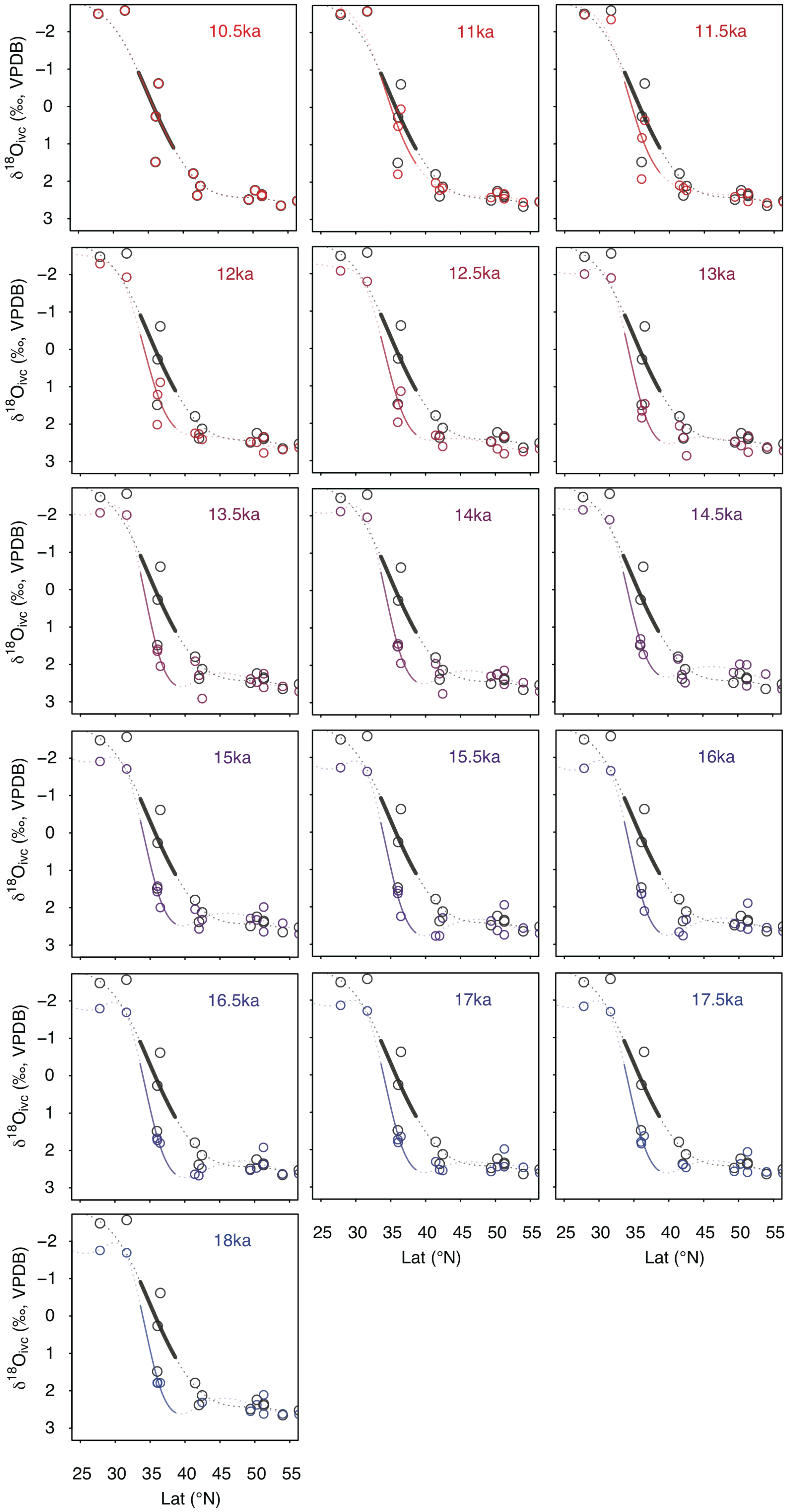

90
91 **Figure S3** As figure S2, however data are from west of 180°.

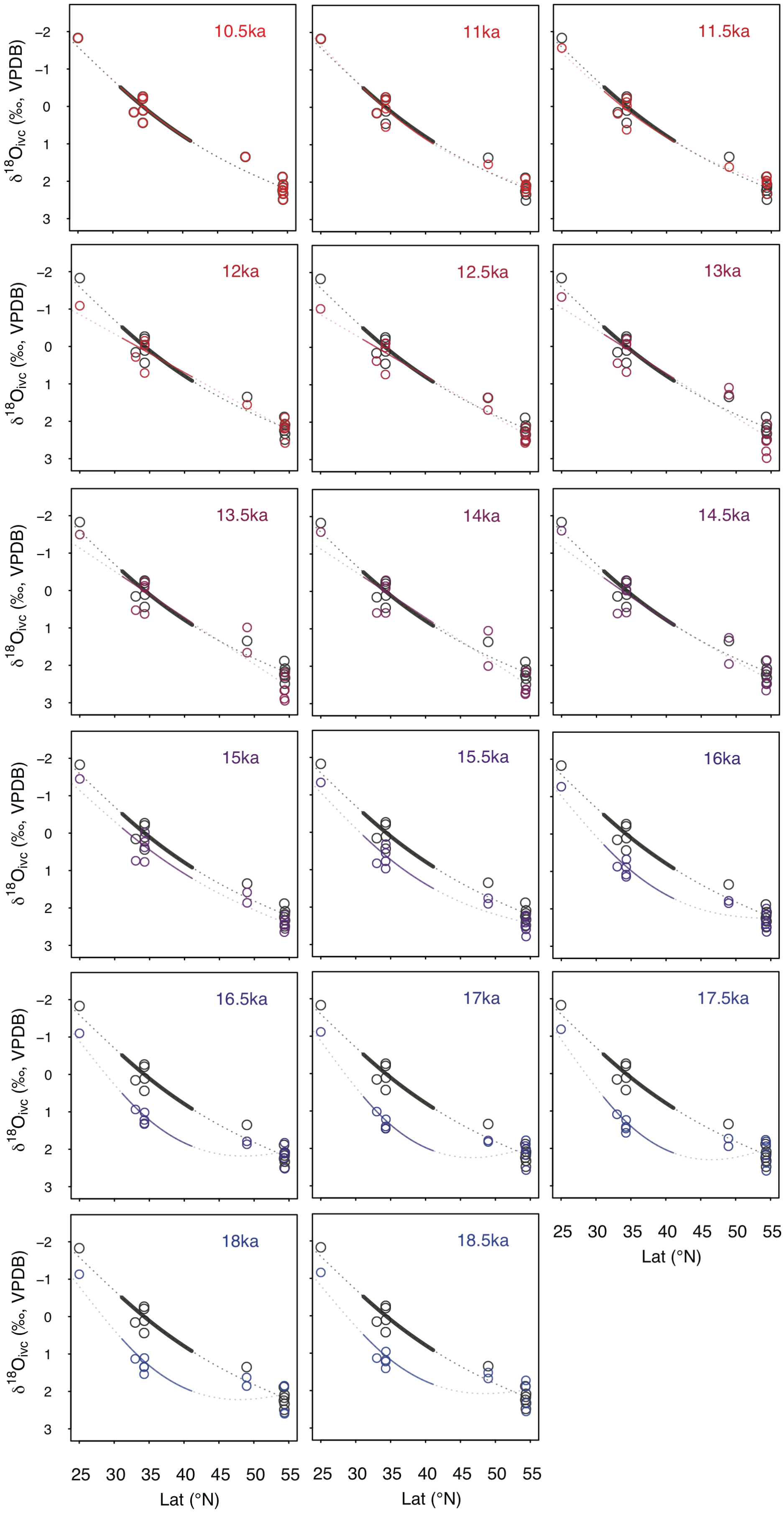

Figure S4 As figure S2, however data are from east of 180°.

We calculate the change in gyre boundary position over deglaciation as the latitudinal shift (x°) that minimises the Euclidean distance (L^2) between the Holocene (taken as 10.5±0.5 ka) $\delta^{18}O_{calcite}$~latitude GAM fit and the GAM fit to each time step, within a latitudinal band spanning the gyre boundary; this latitudinal band is centred around the maximum gradient in $\delta^{18}O_{calcite}$ versus latitude in the Holocene data within a 5° moving window (36.1 °N). In the combined dataset from the east and west, and the data from the west only, we calculate the latitudinal shift using a 5° latitudinal band (i.e. 33.6 to 38.6 °N), and we note the size of this latitudinal band has only a negligible effect on our results (Fig. S5); as the gyre boundary (and thus meridional temperature and $\delta^{18}O_{calcite}$ gradient) is more diffuse in the east, we use a slightly larger window of 10° (i.e. 31.1 to 41.1 °N).

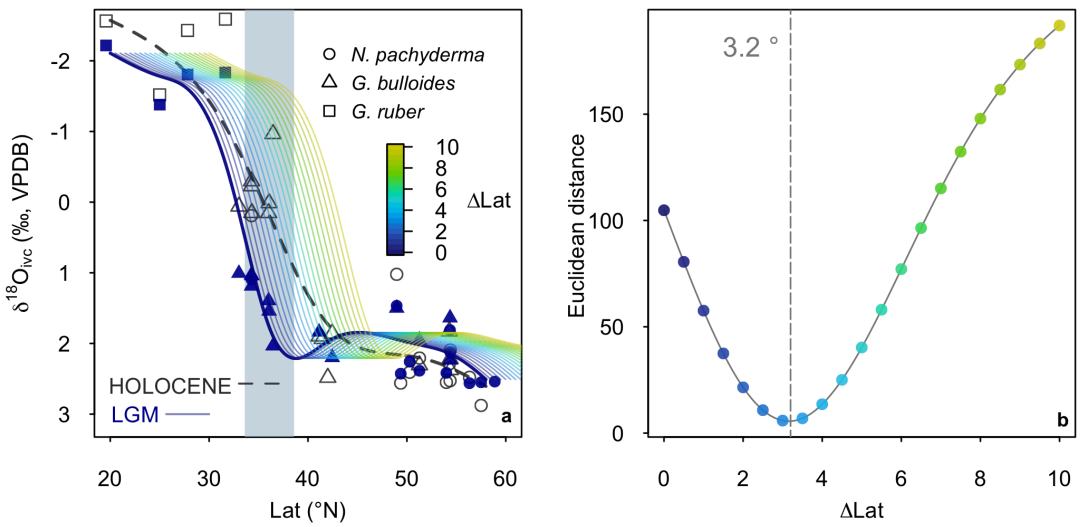

Figure S5 method used to calculate the shift in gyre boundary position **(a)** at each time step (here LGM, 18.5 ka) we calculate the gyre boundary shift as the latitudinal shift (x°, in 0.1 ° increments from 0 to 10 degrees) that minimises the Euclidean distance **(b)** within a specified latitudinal band (grey box in (a) between the GAM fit to the timestep (solid line) and the Holocene (dashed line) in data is calculated. The coloured lines in (a) show the LGM GAM fit shifted north in 0.5° increments, and the coloured dots in (b) show the Euclidean distance from the Holocene line at each increment, with the colour indicating the degree to which the curve has been shifted.

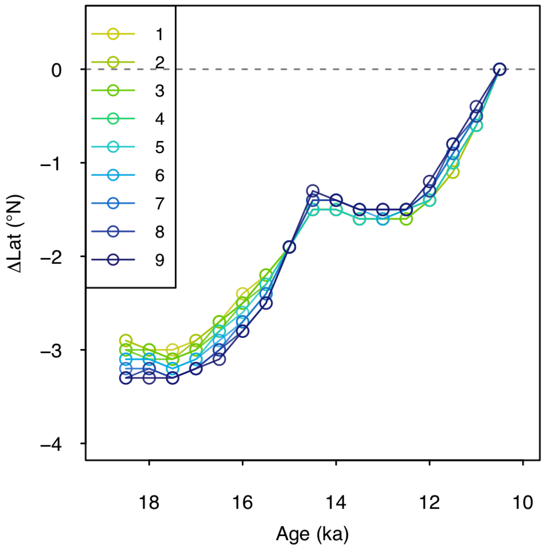

Figure S6 (a) calculated change in the position of the gyre boundary using different sizes of latitudinal band (between 1° and 9°) in which the Euclidean distance between the GAM fits is calculated; the size of latitudinal band (the grey box in figure S5a above) has very little effect on the results.

We note that the steepest part of the Holocene curve (~36.1 °N) using the combined dataset from the east and west, is further south than the zonal mean position of the gyre boundary today (~40 °N). This is due to the westward bias within the dataset (i.e. there are many more sites in the west relative to the east within the dataset), and the gyre boundary is located slightly further south in the west relative to the zonal mean; the maximum meridional gradient in mean annual SST is found at ~36 °N along the western margin of the basin (Boyer et al., 2013), in good agreement with our reconstruction.

We also note that if we use a totally different method to calculate the change in position of the gyre boundary, simply calculating the change in latitude in the steepest part of the meridional $\delta^{18}O_{calcite}$ gradient (within a 5° moving window), we arrive at a very similar estimate of a ~2.6° southward shift between the Holocene and LGM. This method is more prone to anomalous values at the latitudinal extremes; hence we opt for the method of calculating the latitudinal shift that minimises the Euclidean distance between timesteps within a defined latitudinal band described above. The agreement between the two methods is, however, reassuring.

Planktic foraminiferal $\delta^{18}O_{calcite}$ compilation

We compiled all available planktic foraminiferal calcite $\delta^{18}O$ from cores across the North Pacific. Compiled records include $\delta^{18}O$ measured on *G. ruber*, *G. bulloides*, and *N. pachyderma*. All data were kept on the original age models, except in the case when data were only available on uncalibrated ^{14}C age models, in which case the ^{14}C data were recalibrated using INTCAL13 (Reimer et al., 2013) using an average of the modern reservoir age at each site and a regional glacial increase of +400 years with large uncertainties (±500 years). All $\delta^{18}O_{calcite}$ data along with the core, location, water depth, species, sediment depth, age, and original data reference are given in Table S1. We only include cores spanning the interval between 10.5 to 18.5 ka with an average resolution of >1 point per ka; the average resolution of the individual cores during deglaciation is ~1 point/125 years. We exclude core EW0408-26/66JC from the compilation (Praetorious and Mix, 2014); this core is located in close proximity to the terminus of a glacier, and comparing the $\delta^{18}O_{calcite}$ data of this core to other cores within the subpolar gyre demonstrates planktic foraminiferal $\delta^{18}O_{calcite}$ data from this core primarily reflect local meltwater changes, rather that wider oceanographic conditions in the subpolar gyre (Figure S7). The compiled dataset is given in Dataset S1 and will be available on Pangea.

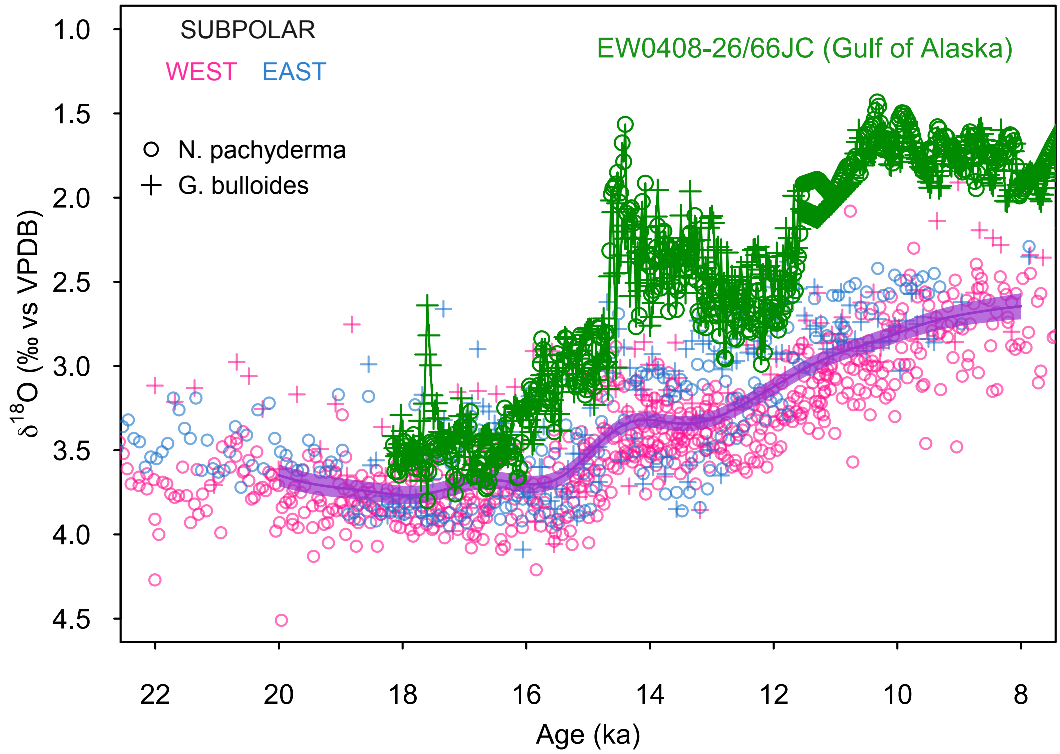

Figure S7 Foraminiferal $\delta^{18}O_{calcite}$ from the subpolar gyre over deglaciation. A GAM fit with to all the data (excluding core EW0408-26/66JC) is shown by the purple line, with 68% Bayesian credible interval shaded. Data from core EW0408-26/66JC (Praetorius and Mix, 2014) is shown in green.

Seasonality of planktic foraminifera

Our approach assumes that any change in seasonal bias relating to the habitat preference of foraminifera are small relative to the change in temperature due to the movement of the gyre boundary. The validity of this approach is supported by sites where $\delta^{18}O_{calcite}$ has been measured on more than one species of foraminifera, such as core ODP Site 893 or MD02-2489 (Figure 1 and Figure 2). At these sites, foraminiferal species with habitat temperature preferences that are known to be different (*G. bulloides* and *N. pachyderma*, e.g. Taylor *et al.*, 2018) show very similar changes down core, with a Holocene-LGM change that is identical (within error); this suggests any changes relating to changes seasonal bias are likely to be insignificant in our reconstruction.

Sea surface temperature and %Opal data

We compiled Mg/Ca and $U^{K'}_{37}$ sea surface temperature (SST) data from across the North Pacific (Mg/Ca: Reitdorf et al., 2013; Gebhardt et al., 2008; Rodriguez Sanz et al., 2013; Taylor et al., 2015; Sagawa et al., 2006; Sagawa et al., 2008; Pak et al., 2012; Kubota et al., 2010; Gray et al, 2018. $U^{K'}_{37}$: Minoshima et al., 2007; Seki, 2004; Harada et al., 2004; Harada, 2006; Harada et al., 2008; Inagaki et al., 2009; Herbert et al., 2001; Sawada et al., 1998; Yamamoto et al., 2004; Isono et al., 2009). All age models are as given in the original publication. All Mg/Ca and $U^{K'}_{37}$ data were recalibrated (see below) and the temperature change during the LGM (Figure 2c) is given as a difference to both proxy temperature in the Holocene, and to mean annual climatological temperature from the WOA13 (Boyer et al., 2013).

While the direct temperature sensitivity of Mg/Ca in planktic foraminifera is ~6% per °C (Gray et al., 2018b; Gray and Evans, 2019), due to the effect of temperature on pH through the disassociation constant of water (K_w), the 'apparent' Mg/Ca temperature sensitivity is higher (Gray et al., 2018b). Thus, we calculate the change in temperature from the change in Mg/Ca at each site using a temperature sensitivity of 8.8%, derived from laboratory cultures (Kisakürek et al., 2008), which encompasses both the direct temperature effect and the temperature-pH effect, with a Mg/Ca-pH sensitivity of ~ -8% per 0.1 pH unit (Lea et al., 1999; Russell et al., 2004; Evans et al., 2016; Gray et al., 2018b; Gray and Evans, 2019). Mg/Ca is also influenced by salinity, with a sensitivity of ~3-4% per PSU (Hönisch et al, 2013; Gray et al., 2018b; Gray and Evans, 2019). As we are primarily interested in (qualitative) changes in meridional SST pattern, we make no attempt to account for the whole ocean effects of salinity or pH downcore. The combined effect of the whole-ocean increase in salinity (due to sea level), and the increase in surface ocean pH (due to lower atmospheric CO_2) means changes in temperature derived from changes in Mg/Ca are likely to be cold-biased by ~1.5 °C during the LGM (Gray and Evans, 2019). For $U^{K'}_{37}$, the change in temperature at each site was calculated using the calibration of Prahl et al., 1988; the temperature range in this study is too low to be substantially effected by the non-linearity of $U^{K'}_{37}$ (e.g. Tierney and Tingley, 2018).

We analyse the North Pacific %Opal compilation of Kohfeld and Chase (2011) to look for qualitative changes in the meridional pattern of productivity over the last deglaciation. Due to the high nutrient supply from upwelling, productivity in the SPG is an order of magnitude higher than the STG. A southward expansion of the gyre boundary should thus result in an increase in productivity within the transition zone; transition zone sites show a ~25% increase in %Opal on both sides of the basin during the LGM (Figure 2d) consistent with nutrient-rich subpolar waters moving further south during the LGM and increasing local productivity.

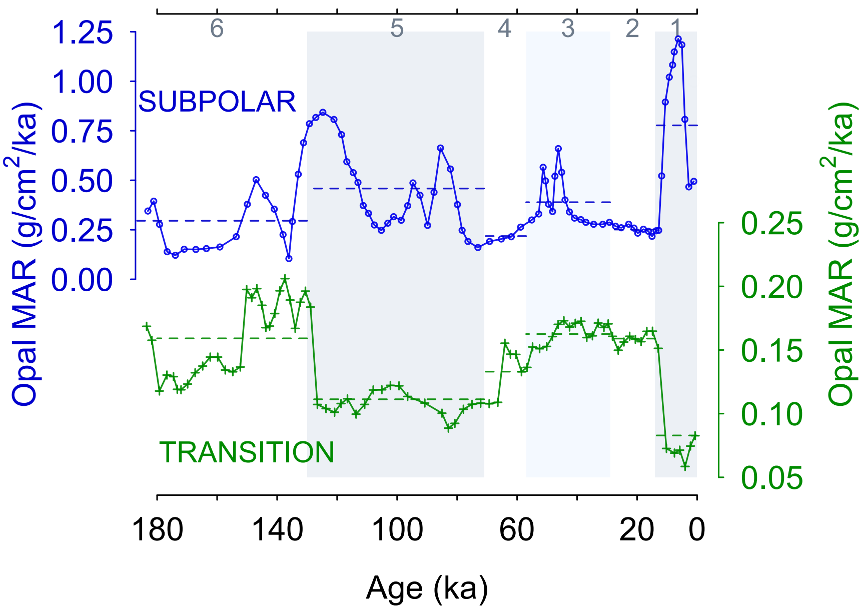

Figure S8 Opal Mass Accumulation Rate data from core KH99-03 in the SPG (Narita et al., 2002) and core NCG108 in the transition zone (Maeda et al., 2002). Dashed lines show mean value for each marine isotope stage (MIS). Grey shading shows MIS 1, 3 and 5. Transition zone and subpolar waters show an anti-phased relationship in Opal MAR over the last glacial cycle.

General Circulation Models

We assess differences in North Pacific barotropic stream function, wind stress curl, zonal wind stress, and SST between LGM and pre-industrial conditions as represented by four coupled climate models (CCSM4, CNRM-CM5, MPI-ESM-P and MRI-CGCM3). All models are part of the Coupled Model Intercomparison Project phase 5 (CMIP5, Taylor et al., 2012). We only used the four models where both wind stress and barotropic stream function data are available. Orbital parameters, atmospheric greenhouse gas concentrations, coastlines and ice topography for the LGM simulations are standardized as part of the Paleoclimate Model Intercomparison Project phase 3 (PMIP3) (Braconnot *et al*. 2012, Taylor *et al*. 2012). Ensemble means are computed by first linearly interpolating to a common grid, and are 4-model means of 100-year climatologies; uncertainties in these centennial averages due to internal variability are negligible.

Using a single model (HadCM3) we look at runs where the model greenhouse gas, ice sheet albedo, ice sheet topography are changed individually ('Green Mountains, White Plains') as described in Roberts and Valdes (2017). The 'Green Mountains, White Plains' runs use the ICE5G ice sheet reconstruction (Peltier *et al*., 2004), whereas the deglacial 'snapshot' runs (below) use the ICE6G ice sheet reconstruction (Peltier *et al*., 2015). The change in gyre boundary position with each forcing are as follows: GHG = -0.5 °N; Albedo = -0.5 °N; Topography = -0.05 °N; Albedo + Topography = -2.4°N; ALL (although with the smaller ICE6G ice sheet) = -3.4 °N.

We also explore changes through time over the deglaciation using a series of HadCM3 equilibrium-type simulations where all forcings and model boundary conditions are changed at 500-year intervals broadly adhering to the PMIP4 last deglaciation protocol (Ivanovic et al., 2016). These simulations use the ICE6GC ice sheet reconstruction and 'melt-uniform' scenario for ice sheet meltwater; i.e. freshwater from the melting ice sheets is NOT routed to the ocean via coastal outlets. Instead, water is conserved by forcing the global mean ocean salinity to be consistent with the change in global ice sheet volume with respect to present. Note, these deglacial simulations are not transient, but are equilibrium-type experiments that begin from the end of the 1750-year long simulations run by Singarayer et al. (2011). At each 500-year interval (21.0 ka, 20.5 ka, 20.0 ka…0.5 ka, 0.0 ka), all boundary conditions and forcings are updated according to the more recent literature (presented by Ivanovic et al., 2016) and held constant for the full 500-year duration of the run. The climate means and standard deviations used here are calculated from the last 50 years of each simulation (i.e. year 451-500, inclusive). More information on these runs can be found in the supplement to Morris et al. (2018), noting that we use the raw model output and not the downscaled and bias-corrected data used in the previous publication. Zonal mean changes in SST anomaly (from global mean), barotropic stream function, and zonal wind stress at each time step are shown below (Fig. S9).

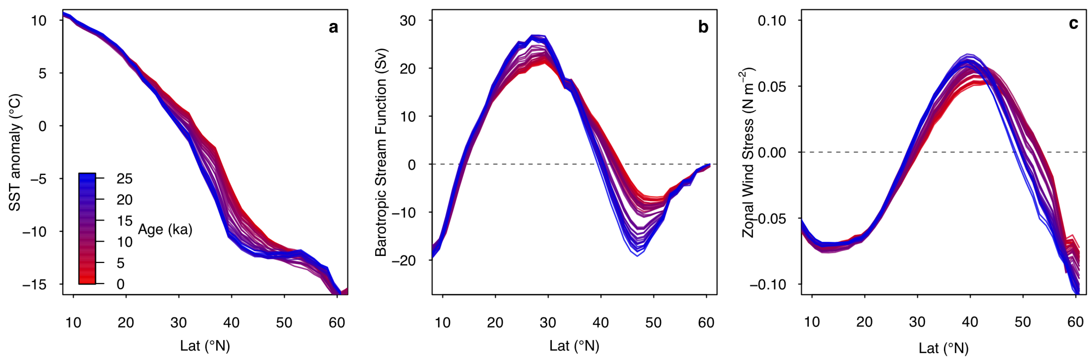

Figure S9 Deglacial evolution of zonal mean **(a)** SST anomaly (relative to global mean) **(b)** barotropic stream function **(c)** zonal wind stress in the HadCM3 simulations.

Eastern boundary test

To test if there is an influence of coastal upwelling on the data in the east (i.e. a signal of some other control on latitudinal temperature anomaly [and thus latitudinal $\delta^{18}O_{calcite}$ anomaly] besides change in gyre position) we compare the ensemble mean SST along the eastern boundary of the basin (taken as the first oceanic grid point west of land during the LGM) to the zonal mean, and zonal mean east of the dateline (Fig. S10). The models show no indication of a strong influence of coastal upwelling, which would manifest as an anomalous cooling relative to the zonal mean. This analysis suggests coastal upwelling is unlikely to be having a significant effect on our results, although the simulated coastal upwelling may be poorly represented due to the resolution of the models.

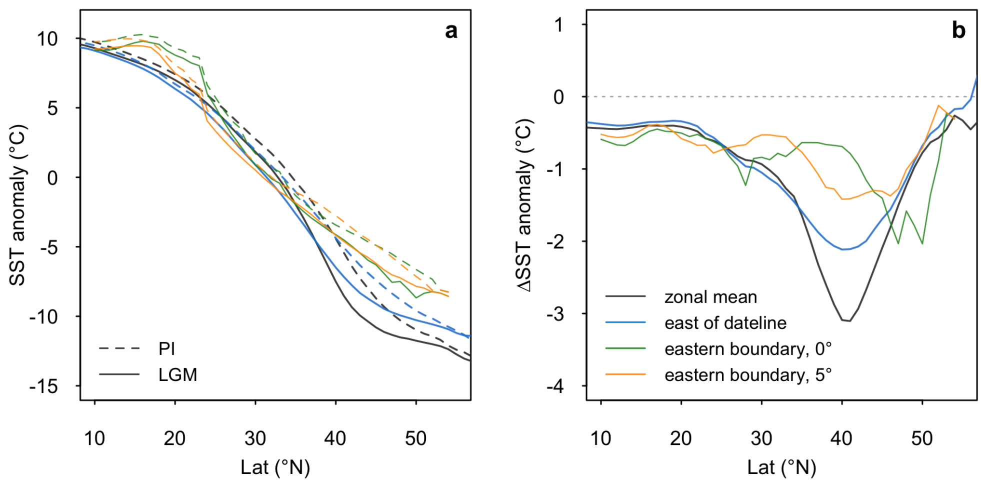

Figure S10 (a) LGM and PI SST anomaly (from global mean), and **(b)** LGM-PI SST anomaly in different longitudinal bins; zonal mean (grey), zonal mean east of the dateline (180°, blue), along the eastern boundary of the basin (green), and 5° seaward from the eastern boundary of the basin (orange). Note, the gyre boundary s located slightly further north along the eastern margin relative to the zonal mean and zonal mean east of the dateline.

HS1 Freshwater test

The release of large amounts of freshwater into the eastern subpolar North Pacific has been suggested over deglaciation, at ~17.5 ka (Maier *et al* 2018). The release of freshwater into the eastern subpolar North Pacific is evident in an increase in the

$\delta^{18}O_{calcite}$ difference between the mixed-layer dwelling species *G. bulloides* and the slightly deeper-dwelling species *N. pachyderma* in core MD02-2489 (54.39°N, -148.92°E) at this time; during this interval *G. bulloides* becomes ~0.6 ‰ more depleted than *N. pachyderma*. To test if this release of freshwater may be influencing our gyre boundary reconstruction we re-run the gyre-boundary analysis, however removing the *G. bulloides* data from core MD02-2489; the results are identical to the gyre boundary reconstruction including the *G. bulloides* data demonstrating that the effect of freshwater release has very little effect on our gyre boundary reconstruction. This is because the change in $\delta^{18}O_{calcite}$ from the freshwater release (~0.6 ‰, equivalent to ~2 PSU freshening) is very small compared to the large change in $\delta^{18}O_{calcite}$ resulting from the temperature difference between the gyres (~5.5 ‰). Localised freshwater inputs, while having a large effect locally, do very little to change the pattern of $\delta^{18}O_{calcite}$ at the basin scale.

Table S1 Compiled planktic foraminiferal $\delta^{18}O_{calcite}$ records. The compiled will be made available on Pangea.

Core	Lat (°N)	Lon (°E)	Species	Reference
MD02-2489	54.39	-148.92	*N. pachyderma*	Gebhardt et al 2008
MD02-2489	54.39	-148.92	*G. bulloides*	Gebhardt et al 2008
PAR87A-10	54.36	-148.46	*G. bulloides*	Zahn et al 1991
PAR87A-10	54.36	-148.46	*N. pachyderma*	Zahn et al 1991
PAR87A-02	54.29	-149.61	*G. bulloides*	Zahn et al 1991
PAR87A-02	54.29	-149.61	*N. pachyderma*	Zahn et al 1991
MD02-2496	48.97	-127.03	*N. pachyderma*	Taylor et al 2015
MD02-2496	48.97	-127.03	*G. bulloides*	Taylor et al 2015
ODP1017	34.32	-121.60	*G. bulloides*	Pak et al 2012
ODP893	34.23	-120.04	*N. pachyderma*	Hendy et al 2002
ODP893	34.23	-120.04	*G. bulloides*	Hendy et al 2002
MD02-2503	34.28	-120.04	*G. bulloides*	Hill et al 2006
AHF-28181	33.01	-119.06	*G. bulloides*	Mortyn et al 1996
MD05-2505	25.00	-112.00	*G. ruber*	Rodríguez-Sanz et al 2013
SO201-2-101	58.88	170.68	*N. pachyderma*	Reitdorf et al 2013
SO201-2-85	57.51	170.41	*N. pachyderma*	Reitdorf et al 2013
SO201-2-77	56.33	170.70	*N. pachyderma*	Reitdorf et al 2013
SO201-2-12	53.99	162.36	*N. pachyderma*	Reitdorf et al 2013
MD01-2416	51.27	167.73	*N. pachyderma*	Gebhardt et al 2008
MD01-2416	51.27	167.73	*G. bulloides*	Gebhardt et al 2008
VINO-GGC37	50.28	167.70	*N. pachyderma*	Keigwin 1998
LV29-114-3	49.34	152.88	*N. pachyderma*	Reitdorf et al 2013
KT90-9_21	42.45	144.32	*G. bulloides*	Oba and Murayama 2004
GH02-1030	42.00	144.00	*G. bulloides*	Sagawa and Ikehara 2008
CH84-14	41.44	142.33	*G. bulloides*	Labeyrie 1996
CH84-04	36.46	142.13	*G. bulloides*	Labeyrie 1996
MD01-2420	36.07	141.82	*G. bulloides*	Sagawa et al 2006
MD01-2421	36.02	141.78	*G. bulloides*	Oba and Murayama 2004
KY07_04_01	31.64	128.94	*G. ruber*	Kubota et al 2010
A7	27.82	126.98	*G. ruber*	Sun et al 2005
ODP184-1145	19.58	117.63	*G. ruber*	Oppo and Sun 2005

Additional References

Boyer, T.P., Antonov, J.I., Baranova, O.K., Coleman, C., Garcia, H.E., Grodsky, A., John- son, D.R., Locarnini, R.A., Mishonov, A.V., O'Brien, T.D., Paver, C.R., Reagan, J.R., Seidov, D., Smolyar, I.V., Zweng, M.M., 2013. World Ocean Database 2013. In: Levitus, Sydney (Ed.), Alexey Mishonov (Technical Ed.), NOAA Atlas NESDIS, vol. 72. 209 pp.

Evans D., Wade B. S., Henehan M., Erez J. and Müller W. (2016) Revisiting carbonate chemistry controls on planktic foraminifera Mg / Ca: Implications for sea surface temperature and hydrology shifts over the Paleocene-Eocene Thermal Maximum and Eocene-Oligocene transition. Clim. Past 12.

Gebhardt, H. et al., Paleonutrient and productivity records from the subarctic North Pacific for Pleistocene glacial terminations I to V. Paleoceanography 23, PA4212 (2008).

Gray, W. R., Weldeab, S., Lea, D. W., Rosenthal, Y., Gruber, N., Donner, B. and Fischer, G. (2018b) The effects of temperature, salinity, and the carbonate system on Mg/Ca in Globigerinoides ruber (white): A global sediment trap calibration. Earth Planet. Sci. Lett. 482, 607–620.

Gray, W.R. and Evans, D. (2019) Nonthermal influences on Mg/Ca in planktonic foraminifera: A review of culture studies and application to the last glacial maximum. Paleoceanography and Paleoclimatology, 34. https://doi.org/10.1029/2018PA003517

Harada, N. Ahagon, N., Uchida, M. (2004) Northward and southward migrations of frontal zones during the past 40 kyr in the Kuroshio-Oyashio transition area. Geochemistry, doi:10.1029/2004GC000740/pdf.

Harada, N. (2006) Rapid fluctuation of alkenone temperature in the southwestern Okhotsk Sea during the past 120 ky. Global and Planetary Change. 53, 29–46.

Harada, N., Sato, M., Sakamoto, T. (2008) Freshwater impacts recorded in tetraunsaturated alkenones and alkenone sea surface temperatures from the Okhotsk Sea across millennial-scale cycles. Paleoceanography. 23, PA3201.

Harada, N., Sato, M., Sakamoto, T. (2008) Freshwater impacts recorded in tetraunsaturated alkenones and alkenone sea surface temperatures from the Okhotsk Sea across millennial-scale cycles. Paleoceanography. 23, PA3201.

Hendy, I. L., Kennett, J. P., Roark, E. B., Ingram, B. L., (2002) Apparent synchroneity of submillenial scale climate events between Greenland and Santa Barbara Basin, California from 30-10 ka. Quaternary Science Reviews 21, 1167-1184.

Herbert, D. et al. (2001) Collapse of the California Current During Glacial Maxima Linked to Climate Change on Land. Science. 293, 71–76.

Hill, T.M., J.P. Kennett, D.K. Pak, R.J. Behl, C. Robert, and L. Beaufort. 2006.Pre-Bolling warming in Santa Barbara Basin, California: surface and intermediate water records of early deglacial warmth. Quaternary Science Reviews 25, pp. 2835–2845, doi:10.1016/j.quascirev.2006.03.012

Hönisch B., Allen K. a., Lea D. W., Spero H. J., Eggins S. M., Arbuszewski J., deMenocal P., Rosenthal Y., Russell A. D. and Elderfield H. (2013) The influence of salinity on Mg/Ca in planktic foraminifers – Evidence from cultures, core-top sediments and complementary δ18O. Geochim. Cosmochim. Acta 121, 196–213.

Inagaki, M., Yamamoto, M., Igarashi, Y., Ikehara, K. (2009) Biomarker records from core GH02-1030 off Tokachi in the northwestern Pacific over the last 23,000 years: Environmental changes during the last deglaciation. Journal of Oceanography. 65, 847–858.

Isono, D. et al. (2009) The 1500-year climate oscillation in the midlatitude North Pacific during the Holocene. Geology. 37, 591–594.

Kisakürek, B., Eisenhauer, A., Böhm, F., Garbe-Schönberg, D., Erez, J., 2008. Controls on shell Mg/Ca and Sr/Ca in cultured planktonic foraminiferan, Globigerinoides ruber (white). Earth Planet. Sci. Lett. 273, 260–269. https://doi.org/10.1016/ j.epsl.2008.06.026.

Kubota, Y., K. Kimoto, R. Tada, H. Oda, Y. Yokoyama, and H. Matsuzaki (2010), Variations of East Asian summer monsoon since the last deglaciation based on Mg/Ca and oxygen isotope of planktic foraminifera in the northern East China Sea, Paleoceanography, 25, PA4205, doi:10.1029/2009PA001891.

Labeyrie, L. 1996. Quaternary paleoceanography: unpublished stable isotope records. IGBP PAGES/World Data Center for Paleoclimatology Data Contribution Series #1996-036. NOAA/NGDC Paleoclimatology Program, Boulder. Colorado, USA.

Lea D. W., Mashiotta T. A. and Spero H. J. (1999) Controls on magnesium and strontium uptake in planktonic foraminifera determined by live culturing. Geochim. Cosmochim. Acta 63, 2369–2379.

Maeda, L., H. Kawahata and M. Noharta (2002): Fluctuation of biogenic and abiogenic sedimentation on the Shatsky Rise in the western north Pacific during the late Quaternary. Marine Geology 189, 197-214.

Minoshima, K., H. Kawahata, K. Ikehara (2007) Changes in biological production in the mixed water region (MWR) of the northwestern North Pacific during the last 27 kyr. Palaeogeography, Palaeoclimatology, Palaeoecology. 254, 430–447.

Mortyn, P. G., Thunell, R. C., Anderson, D. M., Stott, L. D., Le, J. (1996) Sea surface temperature changesin the Southern California Borderlands during the last glacial-interglacial cycle. Paleoceanography 11, 415-430.

Narita, H., M. Sato, S. Tsunogai, M. Maruyama, M. Ikehara, T. Nkatsuka, M. Wakatsuchi, N. Harada and U. Ujiie (2002): Biogenic opal indicating less productive northwestern North Pacific during glacial stages. Geophys. Res. Lett., 29(15), 22-1 to 22-4.

Oba, T., Murayama, M. (2004) Sea-surface temperature and salinity changes in the northwest Pacific since the Last Glacial Maximum. Journal of Quaternary Science 19, 335-346.

Oppo, D. W., and Y. Sun (2005) Amplitude and timing of sea surface temperature change in the northern South China Sea: Dynamic link to the East Asian monsoon. Geology 33, 785–788.

Pak, D. K., D. W. Lea, and J. P. Kennett (2012) Millennial scale changes in sea surface temperature and ocean circulation in the northeast Pacific, 10–60 kyr BP, Paleoceanography 27, PA1212, doi:10.1029/2011PA002238.

Peltier, W. R. (2004). Global glacial isostasy and the surface of the Ice-Age Earth: The ICE-5G (VM2) model and GRACE. Annual Review of Earth and Planetary Sciences, 32(1), 111–149. https://doi.org/10.1146/annurev.earth.32.082503.144359

Praetorius, S. K., Mix, A. C. (2014) Synchronization of North Pacific and Greenland climates preceded abrupt deglacial warming. Science 345, 444. DOI: 10.1126/science.1252000.

Prahl, F. G., L. A. Muehlhausen, and D. L. Zahnle (1988), Further evaluation of long-chain alkenones as indicators of paleoceanographic conditions, Geochim. Cosmochim. Acta 52, 2303–2310.

Reimer, P. J. et al. (2013) IntCal13 and Marine13 radiocarbon age calibration curves 0-50,000 years cal BP. Radiocarbon 55, 1869–1887.

Riethdorf, J.-R., Max, L., Nürnberg, D., Lembke-Jene, L., Tiedemann, R. (2013) Deglacial development of (sub) sea surface temperature and salinity in the subarctic northwest Pacific: Implications for upper-ocean stratification. Paleoceanography. 28, 91–104.

Rodríguez Sanz, L., Mortyn, P. G., Herguera, J. C., Zahn, R. (2013) Hydrographic changes in the tropical and extratropical Pacific during the last deglaciation. Paleoceanography. 28, 529–538.

Russell A. D., Hönisch B., Spero H. J. and Lea D. W. (2004) Effects of seawater carbonate ion concentration and temperature on shell U, Mg, and Sr in cultured planktonic foraminifera. Geochim. Cosmochim. Acta 68, 4347–4361.

Sagawa, T., Toyoda, K., Oba, T. (2006) Sea surface temperature record off central Japan since the Last Glacial Maximum using planktonic foraminiferal Mg/Ca thermometry.

Sagawa, T., Ikehara, K. (2008) Intermediate water ventilation change in the subarctic northwest Pacific during the last deglaciation. Geophysical Research Letters 35, L24702, doi:10.1029/2008GL035133.

Seki, O., et al. (2004)Reconstruction of paleoproductivity in the Sea of Okhotsk over the last 30 kyr. Paleoceanography. 19, PA1016.

Singarayer, J.S., Valdes, P.J., Friedlingstein, P., Nelson, S., Beerling, D.J., 2011. Late Holocene methane rise caused by orbitally controlled increase in tropical sources. Nature 470, 8285. https://doi.org/10.1038/nature09739

Taylor, B.J., Rae, J.W.B., Gray, W.R., Darling, K.F., Burke, A., Gersonde, R., Abelman, A., Maier, E., Esper, O., Ziveri, P. (2018) Distribution and ecology of planktic foraminifera in the North Pacific: Implications for paleo-reconstructions. Quaternary Science Reviews 191, 256-274.

Taylor, M. A., Hendy, I. L., Pak, D. K. (2014) Deglacial ocean warming and marine margin retreat of the Cordilleran Ice Sheet in the North Pacific Ocean. Earth and Planetary Science Letters. 403, 89–98 (2014).

Tierney J. E. and Tingley M. P. (2018) BAYSPLINE: A New Calibration for the Alkenone Paleothermometer. Paleoceanogr. Paleoclimatology 33, 281–301.

Yamamoto, M., Oba, T., Shimamune, J., Ueshima, T. (2004) Orbital-scale anti-phase variation of sea surface temperature in mid-latitude North Pacific margins during the last 145,000 years. Geophysical Research Letters. 31, L16311.

Zahn, R., Pedersen, T. F., Bornhold, B. D., Mix, A. C. (1991) Watermass conversion in the glacial subarctic Pacific (54°N, 148°W): physical constraints and the benthic-planktonic stable isotope record. Paleoceanography 6, 543-560.